Science Advances

AAAS

Supplementary Materials for

Was the moon magnetized by impact plasmas?

Rona Oran*, Benjamin P. Weiss, Yuri Shprits, Katarina Miljković, Gábor Tóth

*Corresponding author. Email: roran@mit.edu

The PDF file includes:

> Supplementary Text
> Figs. S1 to S6
> Table S1
> Legend for movie S1
> References

Other Supplementary Material for this manuscript includes the following:

(available at advances.sciencemag.org/cgi/content/full/6/40/eabb1475/DC1)

> Movie S1

Supplementary Text

1. Solar wind conditions at the time of formation of the large young basins
We seek to estimate the strength of the ambient interplanetary magnetic field (IMF) during the time of the young basin-forming impacts. The ages of the young large basins range between ~3.7-4 Ga ago (*26*) with the Imbrium event occurring sometime between 3.75-3.87 billion years (Ga) ago. As discussed in ref. (*1*), these formation times overlap the period when Apollo sample paleointensities are estimated to have reached tens of μT (i.e., 3.56 to 4.25 Ga ago) (*2*). Using the time of formation of calcium aluminum-rich inclusions (CAIs) as the formation age of the solar system (4.567 Ga ago), we find that the Sun was 0.317 to 1 Ga old at the time when the highest paleointensities were recorded by the Apollo samples and was 0.7-0.8 Ga old at the time of the Imbrium impact.

The solar wind and IMF properties depend on the Sun's surface magnetic field and its rotation period, which changed over time. Their values can be estimated for main sequence stars from stellar evolution and dynamo models (*51*) (Fig. S1 top). To obtain the resulting IMF at 1 AU, we assume the IMF takes the form of the Parker spiral, an Archimedean spiral prescribed by the rotation rate of the Sun and the radial wind speed (Fig. S1 middle). The magnitude of the IMF can then be found from conservation of flux as the wind expands into space (Fig. S1 bottom). There is uncertainty in obtaining the IMF magnitude at 1 AU from the surface field because not all of the solar surface contributes flux to the heliosphere. In Fig. S1 bottom, the green curve shows an extreme upper limit of the IMF at 1 AU obtained by assuming that all the surface flux on the Sun contributes to the IMF due to stretching by the solar wind flow. This is not realistic since the surface magnetic fields of Sun-like stars are sufficiently strong to trap the wind over a considerable fraction of their surfaces, giving rise to closed-field regions. This fraction was likely much lower than 100% for most of the Sun's history. For example, the present-day Sun has only about 30% of its surface covered with open magnetic field lines. For a younger Sun, this fraction is likely even smaller because younger stars have stronger surface fields (*51*). This conclusion is supported by detailed surface field measurements and solar wind modeling of a young stellar object that approximates the Sun at 10 My (*31*). Thus, for a ~300 My Sun, the 30% open-field fraction is an upper limit.

At the formation times of the basins (0.7-0.8 Ga after CAI-formation), we find that the IMF was between 10 nT (assuming a 30% open-field fraction) and ~32 nT (assuming the unrealistic upper limit of a 100% open field fraction (Fig. S1). This range encompasses the 30 nT value suggested by ref. (*20*). We conclude that 30 nT is likely an overestimate of the actual IMF, but nonetheless adopt it to both so we can compare our results with ref. (*20*) as well as to be conservative (such that any amplified field obtained under this assumption would be also an overestimate).
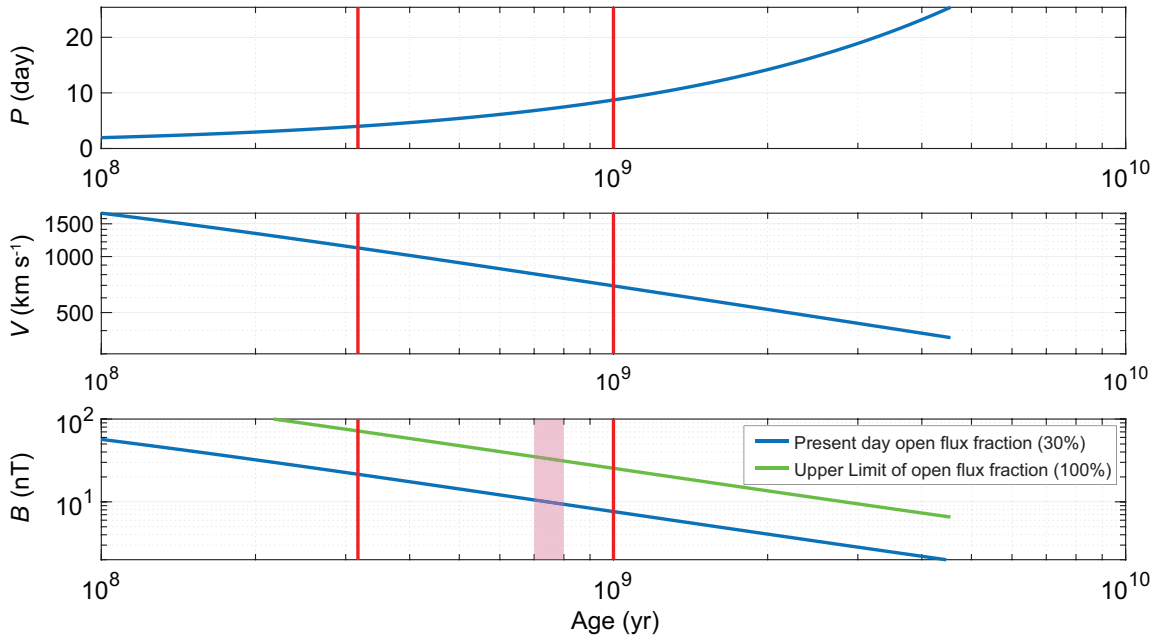
Fig. S1. **Solar wind and IMF conditions over time**. These properties are derived following ref. (*37*) using assumptions detailed in Section 1. Red solid vertical lines mark the ages of 0.317 Ga and 1 Ga after CAI-formation, which correspond to the beginning and end of the high-field epoch when Apollo sample paleointensities reached tens of µT. The shaded light-red rectangle in the bottom panel corresponds to the formation time of the Imbrium-forming event (sometime between 0.7-0.8 Ga after CAI-formation) during which the crustal magnetization antipodal of Imbrium is proposed to have been acquired. (**Top**) Rotation period of the Sun, P, as a function of the Sun's age. (**Middle**) Terminal solar wind speed (the speed the wind achieves at a distance from the Sun where acceleration has already ceased), V, at 1 AU as a function of the Sun's age. (**Bottom**) The magnitude of the IMF, B, at 1 AU as a function of the Sun's age. The green curve represents the IMF magnitude assuming all the surface flux reaches interplanetary space (an extreme upper limit that neglects closed-field regions on the Sun). The blue curve represents the IMF magnitude when assuming a fraction of the solar surface that has open flux equal to that of the present-day Sun. The actual value throughout the Sun's evolution was likely between these two limiting curves.

2. Lunar electrical conductivity profile

The electrical conductivity, σ, of the lunar crust and mantle were measured during the Apollo era (*52*). The conductivity increases with depth, with the crust being orders of magnitude more resistive than the mantle. Typical values for the mantle are $\sigma_{mantle} = 10^{-3}\text{-}10^{-2}$ S m^{-1} and for the crust are $\sigma_{crust} = 1\times10^{-8}$ S m^{-1}.

The conductivity in the core is much higher than in the crust and mantle. According to recent estimates, the Moon formed at ~4.51 Ga ago (*53*) and the core's radius is $r_{core}= 330$ km (*54*). The present-day lunar core is estimated to have an electrical conductivity of $\sigma_{core}= 1.1\text{-}1.5\text{x}10^4$ S m^{-1} (*55*) given the core pressure of 5-6 GPa and temperature of 1000-1600 K. However, at the time of basin formation, the core temperature is estimated to have been 1400-2000 K (*56*). For such temperatures, experiments indicate a pure Fe core at lunar interior pressures will have an electrical conductivity of 10^4 to 10^6 S m^{-1} (*57*). These conductivity values are so large that the core effectively has infinite conductivity given the timescale of our impact simulations (see section 3). As such, we assumed that the core is a perfect conductor in our simulations. The lunar conductivity as a function of depth is depicted in the top panel of Fig. S2.
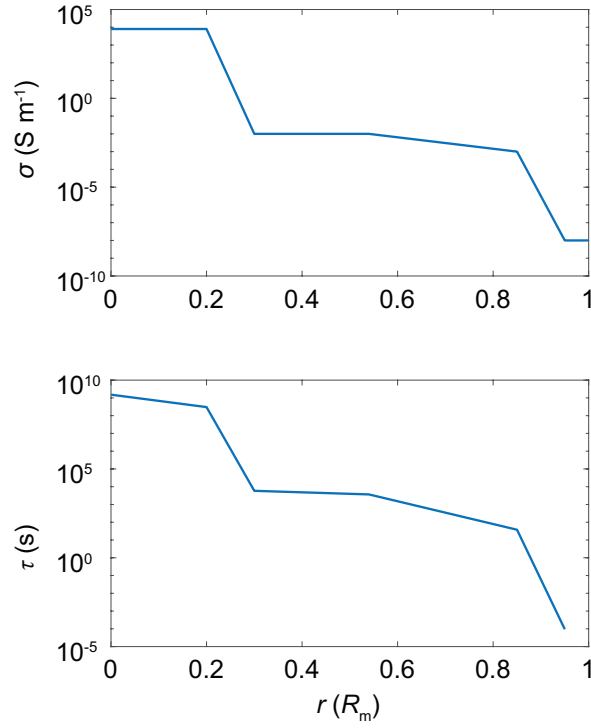
Fig. S2. Conductivity and diffusivity model for the lunar interior. (Top) Electrical resistivity of the Moon as a function of radial distance from the center in units of the lunar radius, R_m. **(Bottom)** The cumulative magnetic diffusion timescale, τ, into each layer.

3. Magnetic dissipation in the crust and removal of magnetic energy after the impact
3.1 The dissipative mechanism
The evolution of the magnetic field inside the Moon is governed by the induction equation:

$$\frac{\partial \boldsymbol{B}}{\partial t} = \frac{1}{\sigma\mu}\nabla^2\boldsymbol{B} \tag{1}$$

where $\boldsymbol{B}$ is the magnetic field vector and μ is the magnetic permeability. For the crust and mantle of the Moon, $\mu \approx \mu_0$ where μ_0 is the permeability of free space (*58*). Note that here we have neglected the displacement current in Ampere's law, an assumption that holds everywhere on the Moon for time scales larger than 0.01 s.

Induction in a resistive medium can give rise, under certain field geometries, to ohmic dissipation such that the total magnetic energy is not conserved but rather converted into heat. The distribution of currents inside the different layers of the Moon during the cloud expansion is complex and constantly changing and is solved directly in the simulations. Here we estimate the loss rate from general physical principles to verify that the simulations are consistent with analytical theory.

Ohmic dissipation can be obtained by dotting Eq. (2) with the magnetic field vector:

$$\boldsymbol{B} \cdot \frac{\partial \boldsymbol{B}}{\partial t} = \frac{1}{\sigma\mu}\boldsymbol{B} \cdot \nabla^2\boldsymbol{B}$$

After some manipulation, this becomes:

$$\frac{1}{2}\frac{\partial B^2}{\partial t} = \frac{1}{\sigma\mu}\left[\frac{1}{2}\nabla^2 B^2 + (\nabla \times \boldsymbol{B})^2\right] \tag{2}$$

Using Ampere's law $\nabla \times \boldsymbol{B} = \mu\boldsymbol{J}$, where $\boldsymbol{J}$ is the current density, this can be written as:

$$\frac{1}{2}\frac{\partial B^2}{\partial t} = \frac{1}{\sigma\mu}\left[\frac{1}{2}\nabla^2 B^2 + (\mu J)^2\right] \tag{3}$$

Recognizing that the magnetic energy density is $E_m = B^2/2\mu$, substituting into Eq. (3) and dividing by μ, we get the time evolution of magnetic energy:

$$\frac{\partial E_m}{\partial t} = \frac{1}{\sigma\mu}\nabla^2 E_m + \frac{1}{\sigma}J^2 \tag{4}$$

Eq. (4) shows that the magnetic energy follows a classic diffusion equation (e.g., for temperature) but with an additional loss term that depends on the magnitude of the currents and the conductivity, often called Joule heating or ohmic dissipation.

The energy density lost to ohmic dissipation per unit time is given by the second term on the right-hand side of Eq. (4):

$$W = J^2/\sigma \tag{5}$$

Ohmic dissipation implicitly occurs in resistive bodies whenever the field is not curl free. Note that a diffusion equation for a scalar quantity (e.g., temperature) would not have this term; it emerges as part of the vector Laplacian in Eq. (1).

3.2 Dissipative power of a given layer in the interior of the Moon
If we assume the conductivity is spherically symmetric, we can estimate the energy lost from ohmic dissipation inside the Moon in a spherical layer spanning from $r = r_1$ to $r = r_2$, where r is the radial distance from the center of the body. If the layer is sufficiently thin, we can assume the conductivity is uniform across the layer and the dissipative power of the layer, W_{layer}, can be calculated exactly:

$$W_{\text{layer}} = \frac{1}{\sigma}\int_V J^2 dV = \frac{4\pi}{\sigma}\int_{r_1}^{r_2} J^2 r^2 dr \tag{6}$$

where the last step represents integration over the spherical shell in the azimuthal and polar directions.

The main change in B would occur between the interior, which initially has magnetic energy corresponding to an induced field of 30 nT, to the cavity created by the expanding vapor, which has a field of < 5 nT. We therefore expect the largest contribution to the current to be derivatives in $\boldsymbol{B}$ in the radial direction, such that the current flows mostly along spherical surfaces. Thus, J can be approximated by:

$$J \cong \frac{\Delta B}{\mu\Delta r}$$

where ΔB is the change in B over a scale length Δr (which may be differ from the layer's thickness). Inserting this into Eq. (6) and integrating, we get the estimated dissipative power:

$$W_{\text{layer}} = \frac{4\pi}{3\sigma\mu^2}(r_2^3 - r_1^3)\left(\frac{\Delta B}{\Delta r}\right)^2 \qquad (7)$$

Layers with high resistivity or those experiencing large changes in B may give rise to strong dissipation and constitute efficient sinks of magnetic energy. This is illustrated in Fig. 1 in the main text and in Fig. S3.

3.3 Estimated dissipation rate and removal time of the initial magnetic energy

The initial magnetic energy inside the Moon, assuming a uniform field of 30 nT induced by the IMF and integrating over the entire body, is 7.8×10^9 J. The magnetic energy in the crust alone (assuming a thickness of ~0.05 R_{m}) is 1.1×10^9 J. These values should be compared to estimates of loss of magnetic energy due to dissipation under the different magnetic configurations reflected in the simulations.

For a crustal conductivity of 10^{-8} S m^{-1}, and taking into account the fact that the cloud expansion exposes the crust to a gradient between 30 nT at its bottom to 3 nT at the surface, we get $\Delta B = 27$ nT and $\Delta r = 0.05\ R_{\text{m}}$ for $r_1 = 0.95\ R_{\text{m}}$ and $r_2 = 1\ R_{\text{m}}$. This gives a dissipative power of the order of 2×10^{13} W in the crust alone, demonstrating that the crust is a very effective dissipator. The initial magnetic energy stored in its inductive currents (due to the solar wind flow) would be cleared almost immediately from regions in the crust adjacent to the magnetic cavity. This dissipative efficiency does not appear under pre-impact conditions: with a constant IMF flow, there is no curl in B in the upwind side such that the magnetic field diffuses through the body almost without loss, while magnetic energy is constantly being replenished by the incoming wind.

In the simulations, we implemented a slightly higher conductivity in the crust in order to ensure numerical stability, of 10^{-6} S m^{-1}. We next verify that the dissipation observed in the simulations is not overestimated by numerical effects. We therefore seek a lower limit estimate of the dissipative power that should emerge from the simulations. First, we relax the assumption that the length scale of changes in the field, Δr, is only as thick as the crust, and instead allow for the smoothest conceivable transition from the initial 30 nT value to the cavity values by setting $\Delta r = 0.8\ R_{\text{m}}$ (that is, by allowing the field to vary smoothly from the core-mantle boundary to the surface). Second, we only consider dissipation by the crust and neglect dissipation within other layers. With these assumptions, we estimate a dissipative power of at least ~7.5×10^8 W, meaning that about 10% of the total initial magnetic energy inside the Moon is converted into heat *every second*. This is consistent with the observed removal of magnetic flux with time in Figs. 1-2 in the main text.

4. Magnetic diffusion timescale and the initial induced field inside the Moon due to solar wind variability

The magnetic diffusion timescale, τ, for a slab of length L, is given by:

$$\tau = \mu\sigma L^2 \qquad (8)$$

The diffusion time as a function of depth is shown in the bottom panel of Fig. S2. The diffusion time allows us to estimate the initial induced field inside the Moon subjected to a changing IMF.

The diffusion timescale through the upper mantle is of the order of hours. It therefore sustains a field similar to typical instantaneous values of the IMF, because large-angle rotations of the IMF occur on a similar timescale (*31*). The diffusion time through the crust will be of the order of fractions of seconds. It too would essentially respond to outside changes (be it the wind or the impact) almost immediately. It therefore does not matter what the field in the crust and upper mantle is initially as it would be washed out quickly with any external change.

S

However, the situation is significantly different for the core, which has a much higher conductivity. The lowest diffusion time through the core is obtained for the lowest conductivity $\sigma_{core} = 1.1\times10^4$ S m^{-1}. Substitution into Eq. (8) yields a core diffusion timescale, τ_{core}, of tens of years. Such a timescale encompasses at least one solar cycle (~22 y for the present-day Sun) and probably more, since stellar activity cycles are shorter for young Sun-like stars (59). Present-day solar wind statistics show that the IMF vector averaged over a solar cycle has a magnitude of about 1% of the mean hourly-averaged IMF magnitude, because of changes in direction on multiple timescales (31). Thus, the magnetic field that diffused into the core at 3.8 Ga ago would average out over the core diffusion timescale and would be only 1% of the young Sun's IMF. In the lower mantle, the diffusion time varies from days to many months; according to ref. (31), the magnitude of the vector average of the IMF over these time scales is 10%-20% of the instantaneous value.

Because the highly resistive crust diffuses magnetic flux on such short time scales, for the purpose of the simulations we implemented a crustal resistivity of $\eta_{crust} = 1\times10^6$ Ω m. This also allows us to achieve numerical stability for larger time steps and cell sizes than those that would be dictated by the real resistivity. This value was chosen such as to enable computationally feasible simulations while ensuring that Moon does not pile up or accumulate the incoming IMF prior to impact (such that the diffusion time scale equals or is shorter than the convection time scale of the solar wind past the Moon).

5. Vapor expansion, shock formation, and cutting off of the solar wind from the Moon

The impact vapor constitutes an obstacle to the wind, causing it to decelerate and pile up. Since the solar wind is super-fast-magnetosonic, its deceleration is accompanied by a shock ahead of the vapor (Fig. S3). At the same time, the vapor continues to be accelerated due to its high pressure, thereby becoming super-fast-magnetosonic. Accordingly, at the edge of the magnetic cavity, the magnetic field becomes larger and a clear transition from superfast to sub-fast flow occurs. As the vapor continues to expand (middle panel of Fig. S3), it sweeps up increasingly more of the incoming IMF, further amplifying the field in the region located between the two flows and their shock fronts. Eventually, the vapor extends over a region large enough such that the hydrodynamic shock of the wind is pushed back and away from the entire Moon. At this point, the sweeping of the IMF by the vapor becomes less effective and the amplification saturates as the Moon becomes disconnected from the IMF.
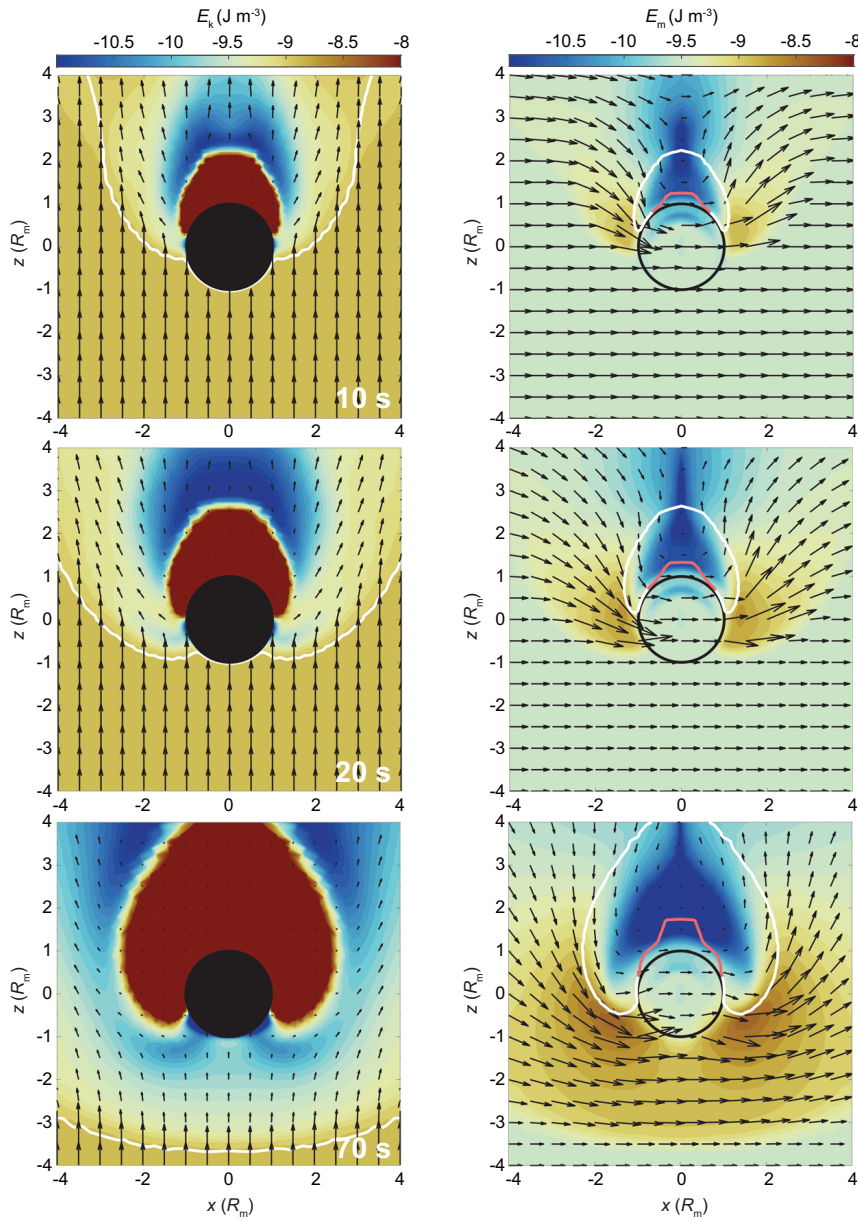
Fig. S3. Conversion of kinetic energy into magnetic energy due to piling up of the solar wind against the impact vapor (Case 1). Shown are snapshots (from top to bottom) taken at 10 s, 20 s, and 70 s after the launch of vapor from the basin. The left column shows the kinetic energy density (color contours) and plasma velocity (black arrows). The white curves in the left column trace the locations where the sonic Mach number, M_s is equal to 1, marking the hydrodynamic shock created by the deceleration of the solar wind. The black circle denotes the Moon. The right column shows the magnetic energy density (color contours) and the magnetic field vector (black arrows). The field points in the direction of the arrows with an intensity proportional to the length of the arrows. The white curves in the right column trace the locations where the fast magnetosonic Mach number, M_f, is equal to one. This marks the transition between the magnetic cavity and the magnetized solar wind where there is a MHD shock. The purple curve inside the cavity marks where the vapor becomes super-fast magnetosonic with $M_f = 1$ due to the gradual increase in its speed; it does not mark a shock.
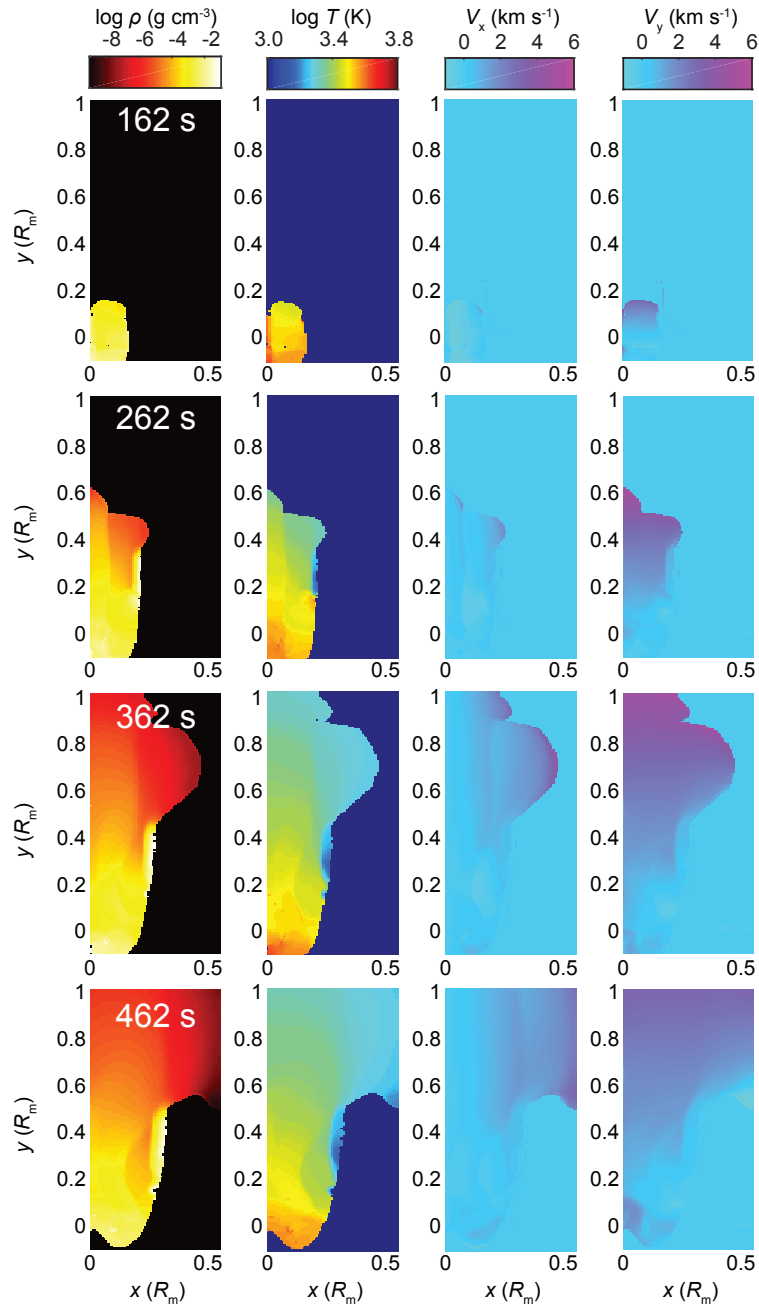
Fig. S4. Results from impact simulations using the iSALE-2D code. Shown are (left to right) the density, temperature, and the x- and y-velocity components at four times (top to bottom) 100 s apart, starting at 162 s after the impact. The x axis is in the horizontal direction and the y axis is in the vertical direction (opposite gravity), representing a cylindrically symmetric physical domain. The initial impact occurs at $(x, y) = (0,0)$. The material shown here only includes vapor (solid and liquid ejecta are not depicted). Distances are shown in units of lunar radii, R_m.
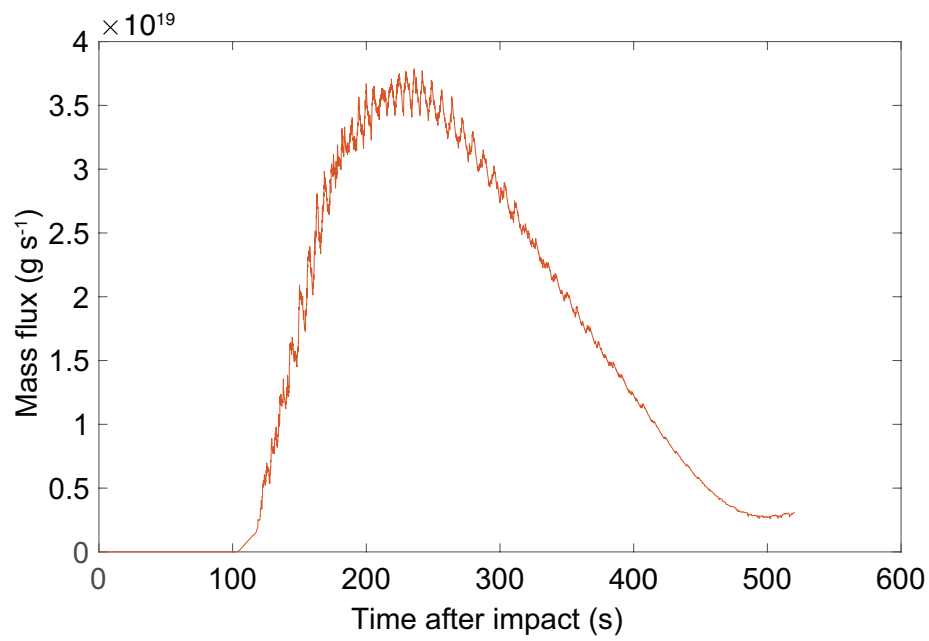
Fig. S5. Total mass rate of vaporized mass coming out of basin as a function of time. These results were obtained by integrating the mass flux through a cross-sectional area that cuts through the basin in Fig. S4 at $y = 0.2\ R_m$, chosen because at this height most vapor is moving upward.
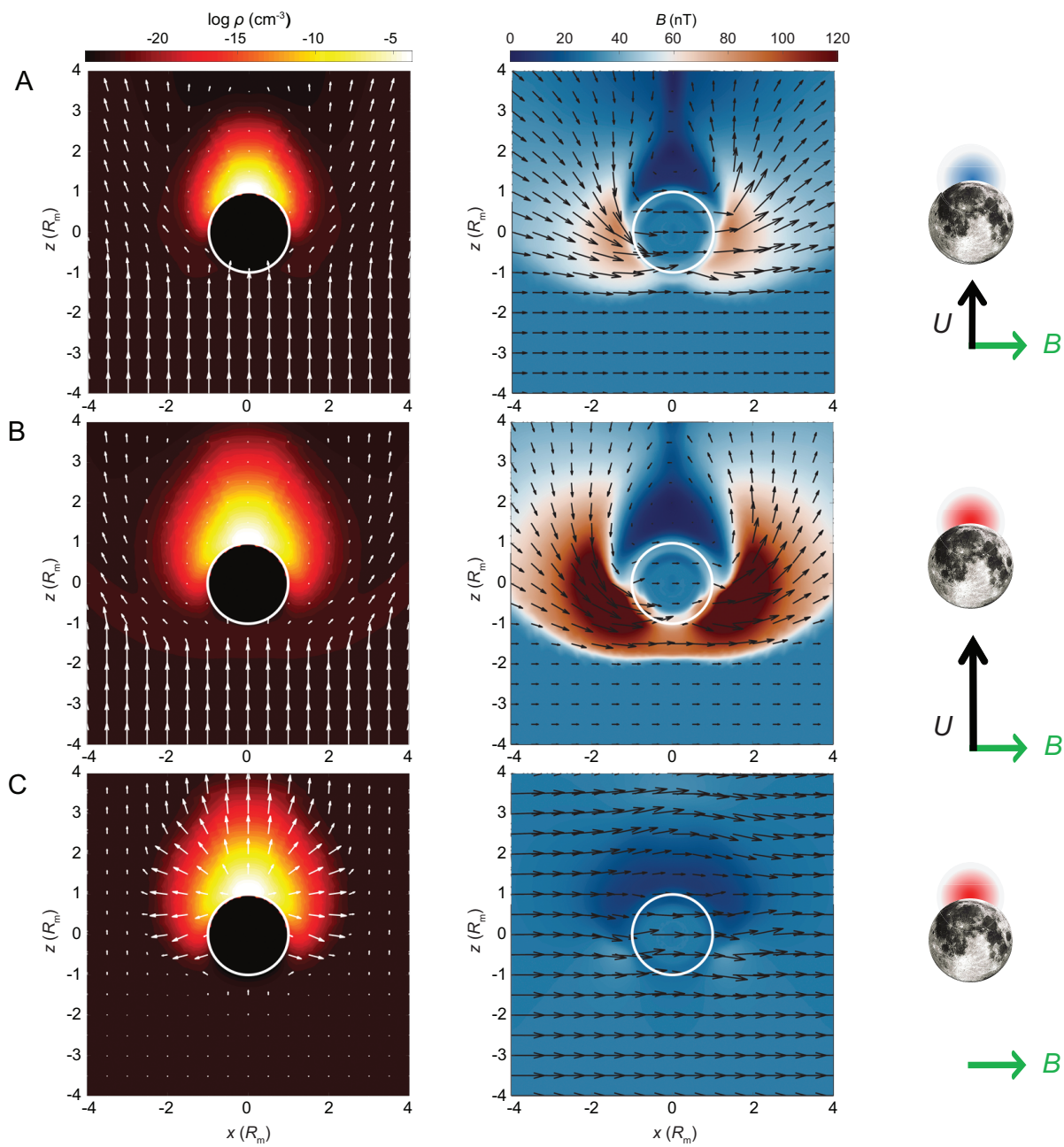
Fig. S6. Plasma flow and magnetic field evolution following different basin-forming impacts on the Moon (Cases 3, 5, and 8). Shown are snapshots from 50 s after the launch of vapor from the basin for the remaining three simulations from Table S1 not included in Fig. 3. Layout, color coding, and symbols are as in Fig. 3. **(A)** Colder initial vapor (Case 3). **(B)** Faster solar wind flow (Case 5). **(C)** No wind flow (Case 8).

Table S1. Summary of the simulations included in the parameter space study.

Case #	Impact location	∂_{IMF} (°)	Additional parameter change	max(B_{surface}) (µT)	Effect on field enhancement
1	wake	90		0.059	
2	upwind	90		0.030	No enhancement inside the body
3	wake	90	Colder vapor (500 K) (slower expansion)	0.067	Longer magnetic link with the compressed wind
4	wake	0	Colder vapor (500 K) (slower expansion)	0.030	No enhancement inside the body
5	wake	90	Faster wind (1000 km s^{-1})	0.096	More compression
6	wake	90	Higher conductivity in the crust and mantle (10^{-2} Ω m)	0.048	Less field changes inside the body
7	wake	90	Faster wind (as in #5) and colder vapor (as in #3)	0.107	More compression, longer magnetic link with the compressed wind
8	Earth's tail	90	No wind	0.044	Little compression

Note: The first column lists the simulation identifier. The second column lists the location of the impact with respect the Sun or Earth. The third column lists the angle the IMF makes with the solar wind flow direction, ∂_{IMF}. The fourth column lists additional parameters that were changed for each simulation. The fifth column lists the maximum magnetic field obtained in this process. The last column includes notes.

Movie S1. Time-dependent plasma flow and magnetic field evolution following a basin-forming impact on the Moon. The movie shows the evolution after the impact described in Case 1 (baseline scenario) in a plane containing the impact vector (–z direction), solar wind flow (+z direction) and the IMF (+x direction). The impact location is at $(x, y, z) = (0, 0, 1)$ R_m. The left panel shows the plasma density (color contours) and velocity (white arrows, scaled to the speed and pointing in flow direction). The right panel shows the magnetic field magnitude (color contours) and vector (black arrows, scaled to magnitude and pointing in field direction). Snapshots from this simulation are shown in Fig. 1.

REFERENCES AND NOTES

1. B. P. Weiss, S. M. Tikoo, The lunar dynamo. *Science* **346**, 1246753 (2014).

2. M. A. Wieczorek, B. P. Weiss, S. T. Stewart, An impactor origin for lunar magnetic anomalies. *Science* **335**, 1212–1215 (2012).

3. A. J. Evans, M. T. Zuber, B. P. Weiss, S. M. Tikoo, A wet, heterogeneous lunar interior: Lower mantle and core dynamo evolution. *J. Geophys. Res.* **119**, 1061–1077 (2014).

4. A. J. Evans, S. M. Tikoo, J. C. Andrews-Hanna. The case against an early lunar dynamo powered by core convection. *Geophys. Res. Lett.* **45**, 98–107 (2018).

5. H. Wang, B. P. Weiss, X.-N. Bai, B. G. Downey, J. Wang, Y. K. Chen-Wiegart, J. Wang, C. Suavet, R. R. Fu, M. E. Zucolotto, Lifetime of the solar nebula constrained by meteorite paleomagnetism. *Science* **355**, 623–627 (2017).

6. L. L. Hood, A. Vickery, Magnetic field amplification and generation in hypervelocity meteoroid impacts with application to lunar paleomagnetism. *J. Geophys. Res.* **89**, C211–C223 (1984).

7. L. L. Hood, Z. Huang, Formation of magnetic anomalies antipodal to lunar impact basins: Two-dimensional model calculations. *J. Geophys. Res.* **96**, 9837–9846 (1991).

8. L. L. Hood, Magnetic field and remanent magnetization effects of basin-forming impacts on the Moon. *Geophys. Res. Lett.* **14**, 844–847 (1987).

9. M. E. Purucker, J. W. Head III, L. Wilson, Magnetic signature of the lunar South Pole-Aitken basin: Character, origin, and age. *J. Geophys. Res.* **117**, E05001 (2012).

10. J. Gattacceca, M. Boustie, L. L. Hood, J.-P. Cuq-Lelandais, M. Fuller, N. S. Bezaeva, T. de Resseguier, L. Berthe, Can the lunar crust be magnetized by shock: Experimental groundtruth. *Earth Planet. Sci. Lett.* **299**, 42–53 (2010).

11. M. A. Wieczorek, B. L. Jolliff, A. Khan, M. E. Pritchard, B. P. Weiss, J. G. Williams, L. L. Hood, K. Righter, C. R. Neal, C. K. Shearer, I. S. McCallum, S. Tompkins, B. R. Hawke, C. Peterson, J. J. Gillis, B. Bussey, The constitution and structure of the lunar interior. *Rev. Mineral. Geochem.* **60**, 221–364 (2006).

12. M. Nayak, D. Hemingway, I. Garrick-Bethell, Magnetization in the South Pole-Aitken basin: Implications for the lunar dynamo and true polar wander, *Icarus* **286**, 153–192 (2017).

13. J. Oliveira, M. A. Wieczorek, G. Kletetschka. Iron abundances in lunar impact basin melt sheets from orbital magnetic field data. *J. Geophys. Res.* **122**, 2429–2444 (2017).

14. D. A. Crawford, P. H. Schultz, Electromagnetic properties of impact-generated plasma, vapor and debris. *Int. J. Impact Eng.* **23**, 169–180 (1999).

15. D. A. Crawford, Simulations of magnetic fields produced by asteroid impact: Possible implications for planetary paleomagnetism. *Int. J. Impact Eng.* **137**, 103464 (2020).

16. G. Chen, T. J. Ahrens, R. Hide, Hypervelocity impacts and magnetization of small bodies in the solar system. *Icarus* **115**, 86–96 (1995).

17. N. Sugiura, M. Lanoix, D. W. Strangway, Magnetic fields of the solar nebula as recorded in chondrules from the Allende meteorite. *Phys. Earth Planet. Inter.* **20**, 342–349 (1979).

18. A. R. Muxworthy, P. A. Bland, T. M. Davison, J. Moore, G. S. Collins, F. J. Ciesla, Evidence for an impact-induced magnetic fabric in Allende, and exogenous alternatives to the core dynamo theory for Allende magnetization. *Meteorit. Planet. Sci.* **52**, 2132–2146 (2017).

19. D. T. Blewett, D. L. Buczkowski, O. Ruesch, J. E. Scully, D. P. O'Brien, R. Gaskell, T. Roatsch, T. J. Bowling, A. Ermakov, H. Hiesinger, D. A. Williams, C. A. Raymond, C. T. Russell, Vesta's north pole quadrangle Av-1 (Albana): Geologic map and the nature of the south polar basin antipodes. *Icarus* **244**, 13–22 (2014).

20. L. L. Hood, N. A. Artemieva, Antipodal effects of lunar basin-forming impacts: Initial 3D simulations and comparisons with observations. *Icarus* **193**, 485–502 (2008).

21. J. Gattacceca, L. Berthe, M. Boustie, F. Vadeboin, P. Rochette, T. De Resseguier, On the efficiency of shock magnetization processes. *Phys. Earth Planet. Inter.* **166**, 1–10 (2008).

22. S. Mighani, H. Wang, D. L. Shuster, C. S. Borlina, C. I. O. Nichols, B. P. Weiss, The end of the lunar dynamo. *Sci. Adv.* **6**, eaax0883 (2020).

23. K. Wünnemann, G. S. Collins, H. J. Melosh, A strain-based porosity model for use in hydrocode simulations of impacts and implications for transient crater growth in porous targets. *Icarus* **180**, 514–527 (2006).

24. G. Tóth, B. der Holst, I. V. Sokolov, D. L. De Zeeuw, T. I. Gombosi, F. Fang, W. B. Manchester, X. Meng, D. Najib, K. G. Powell, Q. F. Stout, A. Glocer, Y.-J. Ma, M. Opher, Adaptive numerical algorithms in space weather modeling. *J. Comput. Phys.* **231**, 870–903 (2012).

25. X. Jia, J. A. Slavin, T. I. Gombosi, L. K. S. Daldorff, G. Toth, B. van der Holst, Global MHD simulations of Mercury's magnetosphere with coupled planetary interior: Induction effect of the planetary conducting core on the global interaction. *J. Geophys. Res.* **120**, 4763–4775 (2015).

26. D. L. Mitchell, J. S. Halekas, R. P. Lin, S. Frey, L. L. Hood, M. H. Acuña, A. Binder, Global mapping of lunar crustal magnetic fields by Lunar Prospector. *Icarus* **194**, 401–409 (2008).

27. M. Le Feuvre, M. A. Wieczorek, Non uniform cratering of the Moon and a revised crater chronology of the inner solar system. *Icarus* **214**, 1–20 (2011).

28. M. A. Wieczorek, G. A. Neumann, F. Nimmo, W. S. Kiefer, G. J. Taylor, H. J. Melosh, R. J. Phillips, S. C. Solomon, J. C. Andrews-Hanna, S. W. Asmar, A. S. Konopliv, F. G. Lemoine, D. E. Smith, M. M. Watkins, J. G. Williams, M. T. Zuber, The crust of the Moon as seen by GRAIL. *Science* **339**, 671–675 (2013).

29. K. Miljković, M. A. Wieczorek, G. S. Collins, M. Laneuville, G. A. Neumann, H. J. Melosh, S. C. Solomon, R. J. Phillips, D. E. Smith, M. T. Zuber, Asymmetric distribution of lunar impact basins caused by variations in target properties. *Science* **342**, 724–726 (2013).

30. J. D. O'Keefe, T. J. Ahrens, Impact-induced energy partitioning, melting, and vaporization on terrestrial planets. *Proc. Eighth Lunar Planet. Sci. Conf.*, 3357–3374 (1977).

31. R. Oran, B. P. Weiss, O. Cohen, Were chondrites magnetized by the early solar wind? *Earth Planet. Sci. Lett.* **492**, 222–231 (2018).

32. E. Kallio, J. G. Luhmann, J. G. Lyon, Magnetic field near Venus: A comparison between Pioneer Venus Orbiter magnetic field observations and an MHD simulation. *J. Geophys. Res.* **103**, 4723–4737 (1998).

33. P. L. Israelevich, A. I. Ershkovich, Induced magnetosphere of comet Halley: 2. Magnetic field and electric currents. *J. Geophys. Res.* **99**, 21225–21232 (1994).

34. K. L. Louzada, B. P. Weiss, A. C. Maloof, S. T. Stewart, N. L. Swanson-Hysell, S. Adam Soule, Paleomagnetism of Lonar impact crater, India. *Earth Planet. Sci. Lett.* **275**, 308–319 (2008).

35. B. P. Weiss, S. Pedersen, I. Garrick-Bethell, S. T. Stewart, K. L. Louzada, A. C. Maloof, N. L. Swanson-Hysell, Paleomagnetism of impact spherules from Lonar crater, India and a test for impact-generated fields. *Earth Planet. Sci. Lett.* **298**, 66–76 (2010).

36. L. Carporzen, B. P. Weiss, S. A. Gilder, A. Pommier, R. J. Hart, Lightning remagnetization of the Vredefort impact crater: No evidence for impact-generated magnetic fields, *J. Geophys. Res.* **117**, E01007 (2012).

37. S. A. Gilder, J. Pohl, M. Eitel, Magnetic signatures of terrestrial meteorite impact craters: A summary, in *Magnetic Fields in the Solar System,* H. Luhr, J. Wicht, S.A. Gilder, M. Holschneider, Eds. (Springer, 2018), pp 357–382.

38. C. A. Dwyer, D. J. Stevenson, F. Nimmo, A long-lived lunar dynamo driven by continuous mechanical stirring. *Nature* **479**, 212–214 (2011).

39. C. Stys, M. Dumberry, A past lunar dynamo thermally driven by the precession of its inner core. *J. Geophys. Res.* **125**, e2020JE006396 (2020).

40. A. L. Scheinberg, K. M. Soderlund, L. T. Elkins-Tanton, A basal magma ocean dynamo to explain the early lunar magnetic field. *Earth Planet. Sci. Lett.* **492**, 144–151 (2018).

41. A. Amsden, H. Ruppel, C. Hirt, "SALE: A simplified ALE computer program for fluid flow at all speeds" (Report LA-8095, Los Alamos National Laboratory, 1980).

42. H. J. Melosh, E.V. Ryan, E. Asphaug, Dynamic fragmentation in impacts: Hydrocode simulation of laboratory impacts. *J. Geophys. Res.* **97**, 14735–14759 (1992).

43. B. A. Ivanov, D. Deniem, G. Neukum, Implementation of dynamic strength models into 2D hydrocodes: Applications for atmospheric breakup and impact cratering. *Int. J. Impact Eng.* **20**, 411–430 (1997).

44. G. S. Collins, H. J. Melosh, B. A. Ivanov, Modeling damage and deformation in impact simulations. *Meteorit. Planet. Sci.* **39**, 217–231 (2004).

45. G. S. Collins, H. J. Melosh, K. Wünnemann, Improvements to the ε-α compaction model for simulating impacts into high-porosity solar system objects. *Int. J. Impact Eng.* **38**, 434–439 (2011).

46. G. S. Collins, Numerical simulations of impact crater formation with dilatancy. *J. Geophys. Res.* **119**, 2600–2619 (2014).

47. E. Pierazzo, A. M. Vickery, H. J. Melosh, A reevaluation of impact melt production. *Icarus* **127**, 408–424 (1997).

48. D. Elbeshausen, K. Wünnemann, G. S. Collins, Scaling of oblique impacts in frictional targets: Implications for crater size and formation mechanisms. *Icarus* **204**, 716–731 (2009).

49. R. W. K. Potter, G. S. Collins, W. S. Kiefer, P. J. McGovern, D. A. Kring, Constraining the size of the South Pole-Aitken basin impact. *Icarus* **220**, 730–743 (2012).

50. F. Crameri, Geodynamic diagnostics, scientific visualisation and StagLab 3.0. *Geosci. Model Dev.* **11**, 2541–2562 (2018).

51. G. Newkirk Jr., Solar variability on time scales of 10^5 to the 5th years to $10^{9.6}$ years, in *The Ancient Sun: Fossil Record in the Earth, Moon and Meteorites* (Pergamon Press, 1980), pp. 293–320.

52. P. Dyal, C. W. Parkin, W. D. Daily, Global lunar crust: Electrical conductivity and thermoelectric origin of remanent magnetism. *Proc. Lunar Planet. Sci. Conf.*, 767–783 (1977).

53. M. Barboni, P. Boehnke, B. Keller, I. E. Kohl, B. Schoene, E. D. Young, K. D. McKeegan, Early formation of the Moon 4.51 billion years ago. *Sci. Adv.* **3**, e1602365 (2017).

54. R. C. Weber, P.-Y. Lin, E. J. Garnero, Q. Williams, P. Lognonné, Seismic detection of the lunar core. *Science* **331**, 309–312 (2011).

55. R. A. Secco, H. H. Schloessin, The electrical resistivity of solid and liquid Fe at pressures up to 7 GPa, *J. Geophys. Res.* **94**, 5887–5894 (1989).

56. N. Zhang, E. M. Parmentier, Y. Liang, A 3-D numerical study of the thermal evolution of the Moon after cumulate mantle overturn: The importance of rheology and core solidification. *J. Geophys. Res.* **118**, 1789–1804 (2013).

57. M. Berrada, R. A. Secco, W. Yong, J. A. H. Littleton, Electrical resistivity measurements of Fe-Si with implications for the early lunar dynamo. *J. Geophys. Res.* **125**, e2020JE006380 (2020).

58. P. Dyal, C. W. Parkin, W. D. Daily, Lunar electrical conductivity and magnetic permeability. *Proc. Lunar Planet. Sci. Conf.*, 2909–2926 (1975).

59. T. S. Metcalfe, R. Egeland, J. Van Saders, Stellar evidence that the solar dynamo may be in transition. *Astrophys. J. Lett.* **826**, L2 (2016).